Journal of Computational Physics 365 (2018) 56–73

Contents lists available at ScienceDirect

Journal of Computational Physics

www.elsevier.com/locate/jcp

Efficient energy stable schemes for isotropic and strongly anisotropic Cahn–Hilliard systems with the Willmore regularization

Ying Chen [a,*], John Lowengrub [b], Jie Shen [c], Cheng Wang [d], Steven Wise [e]

[a] Department of Mathematics, Duke University, Durham, NC 27708, United States
[b] Department of Mathematics, University of California, Irvine, Irvine, CA 92697, United States
[c] Department of Mathematics, Purdue University, West Lafayette, IN 47906, United States
[d] Department of Mathematics, University of Massachusetts, North Dartmouth, MA 02747, United States
[e] Department of Mathematics, University of Tennessee, Knoxville, TN 37996, United States

ARTICLE INFO

Article history:
Received 11 May 2017
Received in revised form 3 March 2018
Accepted 14 March 2018
Available online 16 March 2018

Keywords:
Phase-field
Cahn–Hilliard
Anisotropy
Willmore regularization
Energy stable
Multigrid method

ABSTRACT

We develop efficient energy stable numerical methods for solving isotropic and strongly anisotropic Cahn–Hilliard systems with the Willmore regularization. The scheme, which involves adaptive mesh refinement and a nonlinear multigrid finite difference method, is constructed based on a convex splitting approach. We prove that, for the isotropic Cahn–Hilliard system with the Willmore regularization, the total free energy of the system is non-increasing for any time step and mesh sizes. A straightforward modification of the scheme is then used to solve the regularized strongly anisotropic Cahn–Hilliard system, and it is numerically verified that the discrete energy of the anisotropic system is also non-increasing, and can be efficiently solved by using the modified stable method. We present numerical results in both two and three dimensions that are in good agreement with those in earlier work on the topics. Numerical simulations are presented to demonstrate the accuracy and efficiency of the proposed methods.

© 2018 Published by Elsevier Inc.

1. Introduction

Phase field methods have been widely used to study the dynamics of different material phases via order parameters, such as phase transformations in binary alloys, e.g., [22,19,20]; epitaxial thin film growth, e.g., [15,44,26,35,34,46]; crystal faceting, e.g., [36,27,28,7]; multiphase fluid flow, e.g., [23,2,3,12]; and solid tumor growth, e.g., [43,42,13,11], just to name a few. The methods are capable of describing the evolution of complex, morphology-changing surfaces and can provide a general framework to consider more physical effects. The well-studied second order Allen–Cahn [1] and fourth order Cahn–Hilliard models [8] are sub-classes of phase field models, which are of interest in materials science.

Crystalline anisotropy is a critical contributing factor to the equilibria and dynamic macroscopic shapes of heterogeneous materials. In the absence of anisotropy, the microscopic shape is rotationally symmetric. Anisotropy breaks this symmetry as certain directions are endowed with higher energy. For sufficiently strong anisotropy, the double-well surface density function may become negative. At equilibrium, the system responds by removing these orientations (termed

* Corresponding author.
E-mail addresses: yingc@math.duke.edu (Y. Chen), lowengrb@math.uci.edu (J. Lowengrub), shen@math.purdue.edu (J. Shen), cwang1@umassd.edu (C. Wang), swiss1@utk.edu (S. Wise).

https://doi.org/10.1016/j.jcp.2018.03.024
0021-9991/© 2018 Published by Elsevier Inc.

missing orientations) in the shape of the crystal (Wulff shape) driven by minimizing the total surface energy of the system. As a result, the equilibrium interface is no longer a smooth curve, but presents sharp corners or facets with slope discontinuities [33]. In three dimensions, the onset of missing orientations occurs at a convex-to-concave transition in a polar plot of the reciprocal of the surface free energy (γ) [29], which is equivalent to show that the normal to the $1/\gamma$-plot is proportional to the ξ vector in [9]. The anisotropic phase field model becomes ill-posed when the gradient energy is non-convex, which is equivalent with the sign change of the surface stiffness [33,41]. To overcome ill-posedness and loss of smoothness of the anisotropic Cahn–Hilliard model, a higher order derivative regularization is added to the surface energy [14,6]. For example, a Laplacian-squared regularization is used in [41,10], and a nonlinear Willmore regularization is considered in [35,10,27,28]. Recently, some theoretical studies of the regularized Cahn–Hilliard equation have been conducted. For instance, well-posedness for the isotropic Cahn–Hilliard equation with Willmore regularization was shown in [25], and the proof of existence and uniqueness of the solution to the strongly anisotropic Cahn–Hilliard equation with Willmore regularization was obtained in [24]. For both regularizations, the resulting Cahn–Hilliard-type equations are sixth order in space, which bring significant challenges in the development of efficient and accurate numerical schemes.

Eggleston et al. [16] used a convexification technique for the strongly anisotropic Cahn–Hilliard system and performed one-sided difference approximation to treat the corners to maintain the stability of the numerical method. The simulation results showed excellent agreement with sharp interface equilibrium shapes. However, the use of explicit time discretization leaded to severe time step restrictions. Torabi et al. [35] implemented finite difference in space and a Crank–Nicholson scheme to discretize in time. Recently, a stabilized time discretization and spectral discretization in space were used to solve the regularized anisotropic Cahn–Hilliard equation in [10]. This scheme is unconditionally energy stable.

As a first step towards the development of a scheme for the anisotropic system, we first develop an energy stable time discretization scheme based on a convex splitting approach for the isotropic Cahn–Hilliard–Willmore system, and prove that it is unconditionally energy stable. For the spatial discretization, we use centered finite difference method with a dynamic, block-structured Cartesian mesh refinement. An adaptive nonlinear multigrid method is used to solve the resulting nonlinear system at each time step [41,43,42,13]. We note that the convex splitting we use here is different from that used in [18] which was intended for the functionalized Cahn–Hilliard equation but can also be used for the isotropic Cahn–Hilliard–Willmore equation. However, we encountered difficulty in implementing the nonlinear multigrid method using the scheme in [18] for the isotropic Cahn–Hilliard–Willmore equation.

We then extend this scheme to the strongly anisotropic Cahn–Hilliard system with the Willmore regularization. We present numerical results in 2D and 3D to show that the scheme is still energy stable with arbitrary time steps, although we are not able to prove this analytically.

This paper is organized as follows. In Section 2, we describe the isotropic Cahn–Hilliard and strongly anisotropic Cahn–Hilliard systems with the Willmore regularization. In Section 3, we proposed energy stable numerical methods based on a convex splitting approach for solving the model systems. Two and three dimensional numerical simulations and a summary are presented in Section 4.

2. Diffuse interface anisotropy

Here, we consider a boundary domain $\Omega \subset \mathbb{R}^d$ with $d = 2, 3$. Let $\phi : \Omega \to \mathbb{R}$ be an order parameter; $\mathbf{n} = \frac{\nabla\phi}{|\nabla\phi|}$ is the unit normal vector, and $\mathbf{P} = \mathbf{I} - \mathbf{n} \otimes \mathbf{n}$, where $\mathbf{I}$ is the identity matrix. We consider an anisotropic surface energy [35] as

$$E(\phi) = \int_\Omega \frac{\gamma(\mathbf{n})}{\epsilon}\Big(f(\phi) + \frac{\epsilon^2}{2}|\nabla\phi|^2\Big)d\mathbf{x}, \tag{1}$$

where ϵ is a small parameter that measures the thickness of the interface transition layer, $f(\phi) = \frac{1}{4}\phi^2(1-\phi)^2$ is a double well potential, $\gamma(\mathbf{n})$ is an interfacial energy function describing the property of the anisotropy. Note that the interface thickness is independent of orientation. This is a natural formulation if we interpret the term $\frac{1}{\epsilon}(f(\phi) + \frac{\epsilon^2}{2}|\nabla\phi|^2)$ as the approximation of the surface delta function. The corresponding evolution equations are as follows:

$$\frac{\partial\phi}{\partial t} = \frac{1}{\epsilon}\nabla\cdot(M(\phi)\nabla\mu), \tag{2}$$

$$\mu = \frac{1}{\epsilon}(\gamma(\mathbf{n})f'(\phi) - \epsilon^2\nabla\cdot\mathbf{m}), \tag{3}$$

with

$$\mathbf{m} = \gamma(\mathbf{n})\nabla\phi + \mathbf{P}\nabla_n\gamma(\mathbf{n})\Big(\frac{f(\phi)}{\epsilon^2|\nabla\phi|} + \frac{1}{2}|\nabla\phi|\Big). \tag{4}$$

Following [35], we use the asymptotic result that near interface $f(\phi) \sim (\epsilon^2/2)|\nabla\phi|^2$, to yield the approximation

$$\mathbf{m} \sim \gamma(\mathbf{n})\nabla\phi + |\nabla\phi|\mathbf{P}\nabla_n\gamma(\mathbf{n}). \tag{5}$$

The difference between an isotropic system and an anisotropic one is the choice of $\gamma(\mathbf{n})$ in Eq. (1). When $\gamma(\mathbf{n}) = 1$, the system is isotropic and the free energy does not depend on orientation. In this case, the H^{-1}-gradient flow of Eq. (1) leads to the usual isotropic Cahn–Hilliard equation. In the anisotropic case, $\gamma(\mathbf{n})$ depends on $\mathbf{n}$ in the nontrivial manner. For example, a four-fold symmetric anisotropy can be modeled using [29]:

$$\gamma(\mathbf{n}) = 1 + \alpha\Big(4\sum_{i=1}^{d} n_i^4 - 3\Big), \tag{6}$$

where α describes the anisotropic strength and $d = 2, 3$. In two dimensions, this is equivalent to

$$\gamma(\mathbf{n}) = 1 + \alpha\cos(4\theta), \tag{7}$$

where θ denotes the angle between the normal vector to the interface and the x-axis. When $\alpha = 0$, the system is isotropic. As α increases, the system becomes anisotropic. A sufficient large α would produce a strongly anisotropic system, and the Cahn–Hilliard equation would become ill-posed. In order to overcome the ill-posedness, one may add an extra term to regularize the system. In this paper, we add a nonlinear Willmore energy as a regularization. The regularized free energy thus reads

$$E(\phi) = \int_\Omega \frac{\gamma(\mathbf{n})}{\epsilon}\Big(f(\phi) + \frac{\epsilon^2}{2}|\nabla\phi|^2\Big) + \frac{\beta}{2}\frac{1}{\epsilon^3}(f'(\phi) - \epsilon^2\Delta\phi)^2 d\mathbf{x}, \tag{8}$$

where β represents the bending rigidity. Taking the H^{-1}-gradient flow on the new energy (8), we derive a strongly anisotropic Cahn–Hilliard system with the Willmore regularization:

$$\frac{\partial\phi}{\partial t} = \frac{1}{\epsilon}\nabla\cdot(M(\phi)\nabla\mu), \tag{9}$$

$$\mu = \frac{1}{\epsilon}(\gamma(\mathbf{n})f'(\phi) - \epsilon^2\nabla\cdot\mathbf{m}) + \frac{\beta}{\epsilon^2}(f''(\phi)\omega - \epsilon^2\Delta\omega), \tag{10}$$

$$\mathbf{m} = \gamma(\mathbf{n})\nabla\phi + |\nabla\phi|\mathbf{P}\nabla_n\gamma(\mathbf{n}), \tag{11}$$

$$\omega = \frac{1}{\epsilon}(f'(\phi) - \epsilon^2\Delta\phi). \tag{12}$$

This is a sixth-order system. To motivate the development of energy-stable numerical schemes, we first consider an associated regularized isotropic system:

$$E(\phi) = E_s(\phi) + E_b(\phi), \tag{13}$$

with

$$E_s(\phi) = \int_\Omega \frac{1}{\epsilon}(f(\phi) + \frac{\epsilon^2}{2}|\nabla\phi|^2)d\mathbf{x},$$

and

$$E_b(\phi) = \frac{\beta}{2}\int_\Omega \frac{1}{\epsilon^3}(f'(\phi) - \epsilon^2\Delta\phi)^2 d\mathbf{x}.$$

The evolution equations are given below:

$$\frac{\partial\phi}{\partial t} = \frac{1}{\epsilon}\nabla\cdot(M(\phi)\nabla\mu), \tag{14}$$

$$\mu = \frac{1}{\epsilon}(f'(\phi) - \epsilon^2\Delta\phi) + \frac{\beta}{\epsilon^2}(f''(\phi)\omega - \epsilon^2\Delta\omega), \tag{15}$$

$$\omega = \frac{1}{\epsilon}(f'(\phi) - \epsilon^2\Delta\phi). \tag{16}$$

We complete our models with the following boundary conditions:

$$\mathbf{n}\cdot\nabla\phi = \mathbf{n}\cdot\nabla\mu = \mathbf{n}\cdot\nabla\omega = 0. \tag{17}$$

To perform convex splitting, we require the following results.

Lemma 2.1. *Let* $\hat{E}(\phi) = \int_\Omega A((\phi - \frac{1}{2})^4 + |\nabla\phi|^4) + (\phi - \frac{1}{2})^2|\nabla\phi|^2 d\mathbf{x}$. *If* $A \geq 1/2$, *then* $\hat{E}(\phi)$ *is convex.*

Proof. A similar result was proved in [18]. For the reader's convenience, we provide a proof below.

Let $\psi = \phi - \frac{1}{2}$ and define the operators

$$g(\psi) = A(\psi^4 + |\nabla\psi|^4) \quad \text{and} \quad h(\psi) = \psi^2|\nabla\psi|^2. \tag{18}$$

Then we have

$$\hat{E}(\psi) = \int_\Omega g(\psi) + h(\psi)d\mathbf{x}.$$

According to the fact that functions $p(\psi) = \psi^2$ and $q(\psi) = |\nabla\psi|^2$ are convex, which implies

$$\Big(\frac{\psi_1+\psi_2}{2}\Big)^2 \le \frac{\psi_1^2+\psi_2^2}{2}, \tag{19}$$

and

$$\Big|\nabla\Big(\frac{\psi_1+\psi_2}{2}\Big)\Big|^2 \le \frac{|\nabla\psi_1|^2+|\nabla\psi_2|^2}{2}. \tag{20}$$

Using inequalities (19), (20) and through direct calculations, we find

$$\begin{aligned}
&\frac{g(\psi_1)+g(\psi_2)}{2} - g\Big(\frac{\psi_1+\psi_2}{2}\Big) = \frac{A}{2}\Big(\psi_1^4+\psi_2^4+|\nabla\psi_1|^4+|\nabla\psi_2|^4\Big) - A\Big[\Big(\frac{\psi_1+\psi_2}{2}\Big)^4 + \Big|\nabla\Big(\frac{\psi_1+\psi_2}{2}\Big)\Big|^4\Big] \\
&\ge \frac{A}{2}\Big(\psi_1^4+\psi_2^4+|\nabla\psi_1|^4+|\nabla\psi_2|^4\Big) - A\Big[\Big(\frac{\psi_1^2+\psi_2^2}{2}\Big)^2 + \Big(\frac{|\nabla\psi_1|^2+|\nabla\psi_2|^2}{2}\Big)^2\Big] \\
&= \frac{A}{4}\Big[(\psi_1^2-\psi_2^2)^2 + (|\nabla\psi_1|^2-|\nabla\psi_2|^2)^2\Big],
\end{aligned} \tag{21}$$

and

$$\begin{aligned}
&\frac{h(\psi_1)+h(\psi_2)}{2} - h\Big(\frac{\psi_1+\psi_2}{2}\Big) = \frac{1}{2}(\psi_1^2|\nabla\psi_1|^2+\psi_2^2|\nabla\psi_2|^2) - \Big(\frac{\psi_1+\psi_2}{2}\Big)^2\Big|\nabla\frac{\psi_1+\psi_2}{2}\Big|^2 \\
&\ge \frac{1}{2}(\psi_1^2|\nabla\psi_1|^2+\psi_2^2|\nabla\psi_2|^2) - \Big(\frac{\psi_1^2+\psi_2^2}{2}\Big)\Big(\frac{|\nabla\psi_1|^2+|\nabla\psi_2|^2}{2}\Big) \\
&= \frac{1}{4}\Big(\psi_1^2-\psi_2^2\Big)\Big(|\nabla\psi_1|^2-|\nabla\psi_2|^2\Big).
\end{aligned} \tag{22}$$

Adding inequalities (21) and (22) together gives us,

$$\begin{aligned}
&\frac{g(\psi_1)+g(\psi_2)}{2} - g\Big(\frac{\psi_1+\psi_2}{2}\Big) + \frac{h(\psi_1)+h(\psi_2)}{2} - h\Big(\frac{\psi_1+\psi_2}{2}\Big) \\
&= \frac{A}{4}\Big[(\psi_1^2-\psi_2^2)^2 + (|\nabla\psi_1|^2-|\nabla\psi_2|^2)^2\Big] + \frac{1}{4}\Big(\psi_1^2-\psi_2^2\Big)\Big(|\nabla\psi_1|^2-|\nabla\psi_2|^2\Big), \\
&\ge \frac{2A-1}{8}\Big[(\psi_1^2-\psi_2^2)^2 + (|\nabla\psi_1|^2-|\nabla\psi_2|^2)^2\Big].
\end{aligned} \tag{23}$$

The last inequality holds based on the simple fact that $(a+b)^2 \ge 0$, implying $ab \ge -(a^2+b^2)/2$.

It is clearly seen that $A \ge 1/2$ guarantees the convexity of $\hat{E}(\phi)$. □

3. Numerical schemes

3.1. Discrete time and continuous space schemes

In order to solve the isotropic nonlinear Cahn–Hilliard Eqs. (14)–(16), we here develop an energy stable numerical scheme. The scheme, which is first order accurate in time and second order accurate in space, is based on a convex splitting approach, see [17,21,38–40,45,4,5,30,13], and has two important properties: (1) unconditional energy stability, and (2) unconditional unique solvability [40]. The key idea is that the energy E admits a (not necessarily unique) splitting into purely convex and concave energies, that is, $E = E^c - E^e$, where E^c and E^e are convex, though not necessarily strictly convex [17,45], where E^c refers to the contractive part of the energy (convex) and E^e refers to the expansive part of the energy (concave), we consider a canonical splitting of the total free energy of the isotropic system $E(\phi) = E^c(\phi) - E^e(\phi)$ where

$$E^c(\phi) = \int_\Omega \frac{1}{\epsilon}\Big(\frac{1}{4}\Big[(\phi-\frac{1}{2})^4+\frac{1}{16}\Big]+\frac{\epsilon^2}{2}|\nabla\phi|^2\Big)d\mathbf{x} + \int_\Omega \frac{\beta}{2\epsilon^3}\Big((\phi-\frac{1}{2})^6+\frac{1}{16}(\phi-\frac{1}{2})^2+\epsilon^4(\Delta\phi)^2\Big)+\frac{3\beta}{\epsilon}(\phi-\frac{1}{2})^2|\nabla\phi|^2+\frac{3A\beta}{\epsilon}((\phi-\frac{1}{2})^4+|\nabla\phi|^4)d\mathbf{x}, \tag{24}$$

and

$$E^e(\phi) = \int_\Omega \frac{1}{2\epsilon}(\phi-\frac{1}{2})^2 d\mathbf{x} + \int_\Omega \frac{\beta}{4\epsilon^3}(\phi-\frac{1}{2})^4+\frac{\beta}{4\epsilon}|\nabla(\phi-\frac{1}{2})|^2+\frac{3A\beta}{\epsilon}((\phi-\frac{1}{2})^4+|\nabla\phi|^4)d\mathbf{x}. \tag{25}$$

Using standard calculations and Lemma 2.1, it can be shown that both E^c and E^e are convex. Note that the convex splitting above is similar but different from that used in [18] in the case of Cahn–Hilliard–Willmore.

Using this convex splitting, we then propose the following semi-implicit scheme for the isotropic model:

$$\frac{\phi^{k+1}-\phi^k}{s} = \frac{1}{\epsilon}\nabla\cdot(M(\phi^k)\nabla\mu^{k+1}), \tag{26}$$

$$\begin{aligned}\mu^{k+1} = {}& \frac{1}{\epsilon}(\phi^{k+1}-\frac{1}{2})^3-\epsilon\Delta\phi^{k+1}+\frac{\beta}{2\epsilon^3}\Big(6(\phi^{k+1}-\frac{1}{2})^5+\frac{1}{8}(\phi^{k+1}-\frac{1}{2})\Big)+\epsilon\beta\Delta\omega^{k+1}\\ & -\frac{6\beta}{\epsilon}(\phi^{k+1}-\frac{1}{2})\nabla(\phi^{k+1}\nabla\phi^{k+1})+\frac{3\beta}{\epsilon}(\phi^{k+1}-\frac{1}{2})\Delta\phi^{k+1}\\ & +\frac{12A\beta}{\epsilon}((\phi^{k+1}-\frac{1}{2})^3-\nabla\cdot(|\nabla\phi^{k+1}|^2\nabla\phi^{k+1}))\\ & -\frac{1}{\epsilon}(\phi^k-\frac{1}{2})-\frac{\beta}{\epsilon^3}(\phi^k-\frac{1}{2})^3+\frac{\beta}{2\epsilon}\Delta\phi^k-\frac{12A\beta}{\epsilon}((\phi^k-\frac{1}{2})^3-\nabla\cdot(|\nabla\phi^k|^2\nabla\phi^k)),\end{aligned} \tag{27}$$

$$\omega^{k+1} = \Delta\phi^{k+1}. \tag{28}$$

Theorem 3.1. *The energy E is non-increasing in time, i.e., $E(\phi^{k+1}) \le E(\phi^k)$, independent of any choice of the time step size.*

The result follows from the estimate $E(\phi)-E(\psi) \le (\delta_\phi E^c(\phi)-\delta_\phi E^e(\psi), \phi-\psi)_{L^2}$, which was proved by Wise et al. in [45], and taking $\phi=\phi^{k+1}$ and $\psi=\phi^k$. Observe that at the implicit time level the equations are nonlinear but represent the gradients of strictly convex functions. Thus, these equations are uniquely solvable.

Next, we extend this approach to construct a stable scheme for the strongly anisotropic Cahn–Hilliard model (9)–(12). We notice that the term $\gamma(\mathbf{n})$ changes its sign and is a function of phase field parameter ϕ. Thus, it is difficulty to perform a convex splitting of the total energy. Instead, we modify the scheme (26)–(28) to incorporate anisotropy:

$$\frac{\phi^{k+1}-\phi^k}{s} = \frac{1}{\epsilon}\nabla\cdot(M(\phi^k)\nabla\mu^{k+1}), \tag{29}$$

$$\begin{aligned}\mu^{k+1} = {}& \frac{\gamma(\mathbf{n}^k)}{\epsilon}(\phi^{k+1}-\frac{1}{2})^3-\nabla\cdot(\epsilon\gamma(\mathbf{n}^k)\nabla\phi^{k+1})+\frac{\beta}{2\epsilon^3}\Big(6(\phi^{k+1}-\frac{1}{2})^5+\frac{1}{8}(\phi^{k+1}-\frac{1}{2})\Big)+\epsilon\beta\Delta\omega^{k+1}\\ & -\frac{6\beta}{\epsilon}(\phi^{k+1}-\frac{1}{2})\nabla(\phi^{k+1}\nabla\phi^{k+1})+\frac{3\beta}{\epsilon}(\phi^{k+1}-\frac{1}{2})\Delta\phi^{k+1}\\ & +\frac{12A\beta}{\epsilon}((\phi^{k+1}-\frac{1}{2})^3-\nabla\cdot(|\nabla\phi^{k+1}|^2\nabla\phi^{k+1}))\\ & -\frac{\gamma(\mathbf{n}^k)}{\epsilon}(\phi^k-\frac{1}{2})-\epsilon\nabla\cdot(\mathbf{P}\nabla_n\gamma(\mathbf{n}^k)|\nabla\phi^k|)-\frac{\beta}{\epsilon^3}(\phi^k-\frac{1}{2})^3+\frac{\beta}{2\epsilon}\Delta\phi^k\\ & -\frac{12A\beta}{\epsilon}((\phi^k-\frac{1}{2})^3-\nabla\cdot(|\nabla\phi^k|^2\nabla\phi^k)),\end{aligned} \tag{30}$$

$$\omega^{k+1} = \Delta\phi^{k+1}. \tag{31}$$

Although we are not able to prove that this schemes is energy stable, our numerical simulations shown below indicate that the scheme is energy dissipative and stable for any choice of the time step size.

3.2. The fully discrete energy stable schemes

3.2.1. Spatial discretization

We first recall some notation and finite difference operators used in [40,45,12]. We only present the scheme in two dimensions; the three dimensional case is analogously defined. Assuming that the computational domain $\Omega = (0, N_x h) \times (0, N_y h)$, where N_x and N_y are positive integers, and $h > 0$ is the grid spacing. We define

$$x_i = (i - \frac{1}{2})h \quad \text{and} \quad y_j = (j - \frac{1}{2})h,$$

where i, j can take on integer and half integer values. Consider the following three sets of uniform grid points: (i) east-west edge points E^{ew}, (ii) north-south edge points E^{ns}, (iii) cell-centered points C, defined via

$$\begin{aligned}
E^{ew} &= \{(x_{i+\frac{1}{2}}, y_j) | i = 0, \cdots, m;\ j = 1, \cdots, n\},\\
E^{ns} &= \{(x_i, y_{j+\frac{1}{2}}) | i = 1, \cdots, m;\ j = 0, \cdots, n\},\\
\bar{E}^{ew} &= \{(x_{i+\frac{1}{2}}, y_j) | i = 0, \cdots, m;\ j = 0, \cdots, n+1\},\\
\bar{E}^{ns} &= \{(x_i, y_{j+\frac{1}{2}}) | i = 0, \cdots, m+1;\ j = 0, \cdots, n\},\\
C_{m\times n} &= \{(x_i, y_j) | i = 1, \cdots, m;\ j = 1, \cdots, n\},\\
C_{\bar{m}\times n} &= \{(x_i, y_j) | i = 0, \cdots, m+1;\ j = 1, \cdots, n\},\\
C_{m\times \bar{n}} &= \{(x_i, y_j) | i = 1, \cdots, m;\ j = 0, \cdots, n+1\},\\
C_{\bar{m}\times \bar{n}} &= \{(x_i, y_j) | i = 0, \cdots, m+1;\ j = 0, \cdots, n+1\}.
\end{aligned}$$

We define the function spaces

$$\begin{aligned}
\mathcal{C}_{m\times n} &= \{\phi : C_{m\times n} \to \mathbb{R}\}, \qquad & \mathcal{C}_{\bar{m}\times n} &= \{\phi : C_{\bar{m}\times n} \to \mathbb{R}\},\\
\mathcal{C}_{m\times \bar{n}} &= \{\phi : C_{m\times \bar{n}} \to \mathbb{R}\}, \qquad & \mathcal{C}_{\bar{m}\times \bar{n}} &= \{\phi : C_{\bar{m}\times \bar{n}} \to \mathbb{R}\},\\
\mathcal{E}^{ew}_{m\times n} &= \{u : E^{ew} \to \mathbb{R}\}, \qquad & \mathcal{E}^{ns}_{m\times n} &= \{v : E^{ns} \to \mathbb{R}\},\\
\mathcal{E}^{ew}_{m\times \bar{n}} &= \{u : \bar{E}^{ew} \to \mathbb{R}\}, \qquad & \mathcal{E}^{ns}_{\bar{m}\times n} &= \{v : \bar{E}^{ns} \to \mathbb{R}\}.
\end{aligned}$$

To perform the spatial discretization, we replace spatial derivatives by finite difference operators. The reader is referred to [40,45,12] for the definitions of the edge-to-center difference operators $d_x : \mathcal{E}^{ew}_{m\times n} \to \mathcal{C}_{m\times n}$ and $d_y : \mathcal{E}^{ns}_{m\times n} \to \mathcal{C}_{m\times n}$; the center-to-edge average and difference operators $A_x, D_x : \mathcal{C}_{\bar{m}\times n} \to \mathcal{E}^{ew}_{m\times n}$, $A_y, D_y : \mathcal{C}_{m\times \bar{n}} \to \mathcal{E}^{ns}_{m\times n}$, respectively. The Laplacian operator is approximated to second order by

$$\nabla_d^2 \phi_{i,j} = \frac{\phi_{i+1,j} + \phi_{i-1,j} + \phi_{i,j+1} + \phi_{i,j-1} - 4\phi_{i,j}}{h^2}, \tag{32}$$

where ϕ is cell-centered. The Laplacian with non-constant coefficients is approximated to second order by

$$\begin{aligned}
\nabla_d \cdot (m \nabla_d \phi)_{i,j} = &\frac{A_x m_{i+\frac{1}{2},j}(\phi_{i+1,j} - \phi_{i,j}) - A_x m_{i-\frac{1}{2},j}(\phi_{i,j} - \phi_{i-1,j})}{h^2}\\
&+ \frac{A_y m_{i,j+\frac{1}{2}}(\phi_{i,j+1} - \phi_{i,j}) - A_y m_{i,j-\frac{1}{2}}(\phi_{i,j} - \phi_{i,j-1})}{h^2},
\end{aligned} \tag{33}$$

where both ϕ and m are assumed to be cell-centered, and $A_{ave,x}$ and $A_{ave,y}$ are the averaging operators defined componentwise as

$$\begin{aligned}
A_{ave,x} m_{i+\frac{1}{2},j} &= \frac{m_{i+1,j} + m_{i,j}}{2}, \quad & A_{ave,x} m_{i-\frac{1}{2},j} &= \frac{m_{i,j} + m_{i-1,j}}{2},\\
A_{ave,y} m_{i,j+\frac{1}{2}} &= \frac{m_{i,j+1} + m_{i,j}}{2}, \quad & A_{ave,y} m_{i,j-\frac{1}{2}} &= \frac{m_{i,j} + m_{i,j-1}}{2}.
\end{aligned}$$

The grid function norms are defined as follows: for $\phi \in \mathcal{C}_{m\times n}$, $1 \le p < \infty$,

$$\|\phi\|_p = (h^2 \sum_{i=1}^{m} \sum_{j=1}^{n} |\phi_{i,j}|^p)^{1/p}.$$

For any $\phi \in \mathcal{C}_{\bar{m}\times \bar{n}}$, we define

$$\|\nabla_d \phi\|_2 = \sqrt{h^2 [D_x \phi \| D_x \phi]_{ew} + h^2 [D_y \phi \| D_y \phi]_{ns}}.$$

Inner product is define as: for $\phi, \psi \in \mathcal{C}_{m\times n} \cup \mathcal{C}_{\tilde{m}\times n} \cup \mathcal{C}_{m\times \tilde{n}} \cup \mathcal{C}_{\tilde{m}\times \tilde{n}}$,

$$(\phi, \psi)_d = \frac{1}{h^2} \sum_{i=1}^{N_x} \sum_{j=1}^{N_y} \phi_{i,j} \psi_{i,j}.$$

3.2.2. Fully discrete schemes and its properties

We now introduce a fully discrete energy $F : \mathcal{C}_{\tilde{m}\times \tilde{n}} \to \mathbf{R}$, which is consistent with the continuous space energy (13):

$$F(\phi_{i,j}) = F^c(\phi_{i,j}) - F^e(\phi_{i,j}), \tag{34}$$

with

$$\begin{aligned} F^c(\phi) = &\frac{1}{4\epsilon}\|\phi - \frac{1}{2}\|_4^4 + \frac{\epsilon}{2}\|\nabla_d \phi\|^2 + \frac{\beta}{2\epsilon^3}\Big(\|\phi - \frac{1}{2}\|_6^6 + \frac{1}{16}\|\phi - \frac{1}{2}\|_2^2 + \epsilon^4 \|\Delta_d \phi\|^2\Big) + \frac{3A\beta}{\epsilon}\Big(\|\phi - \frac{1}{2}\|_4^4 + \|\nabla_d \phi\|_4^4\Big) \\ &+ \frac{1}{64\epsilon}\text{Area}(\Omega) + \frac{3\beta}{\epsilon}\Big((\phi - \frac{1}{2})^2, |\nabla_d \phi|^2\Big), \end{aligned} \tag{35}$$

and

$$F^e(\phi) = \frac{1}{2\epsilon}\|\phi - \frac{1}{2}\|_2^2 + \frac{\beta}{4\epsilon^3}\|\phi - \frac{1}{2}\|_4^4 + \frac{\beta}{4\epsilon}\|\nabla_d(\phi - \frac{1}{2})\|_2^2 + \frac{3A\beta}{\epsilon}\Big(\|\phi - \frac{1}{2}\|_4^4 + \|\nabla_d \phi\|_4^4\Big), \tag{36}$$

where $\text{Area}(\Omega) = N_x N_y h^2$. F^c and F^e are convex.

The fully discretized version of Eqs. (26)–(28) becomes:

$$\phi_{i,j}^{k+1} - \phi_{i,j}^k = \frac{S}{\epsilon}\nabla \cdot (M(\phi_{i,j}^k)\nabla \mu_{i,j}^{k+1}), \tag{37}$$

$$\begin{aligned} \mu_{i,j}^{k+1} = &\frac{1}{\epsilon}(\phi_{i,j}^{k+1} - \frac{1}{2})^3 - \epsilon \Delta \phi_{i,j}^{k+1} + \frac{\beta}{2\epsilon^3}\Big(6(\phi_{i,j}^{k+1} - \frac{1}{2})^5 + \frac{1}{8}(\phi_{i,j}^{k+1} - \frac{1}{2})\Big) + \epsilon\beta\Delta\omega_{i,j}^{k+1} \\ &- \frac{6\beta}{\epsilon}(\phi_{i,j}^{k+1} - \frac{1}{2})\nabla(\phi_{i,j}^{k+1}\nabla\phi_{i,j}^{k+1}) + \frac{3\beta}{\epsilon}(\phi_{i,j}^{k+1} - \frac{1}{2})\Delta\phi_{i,j}^{k+1} \\ &+ \frac{12A\beta}{\epsilon}((\phi_{i,j}^{k+1} - \frac{1}{2})^3 - \nabla \cdot (|\nabla\phi_{i,j}^{k+1}|^2\nabla\phi_{i,j}^{k+1})) \\ &- \frac{1}{\epsilon}(\phi_{i,j}^k - \frac{1}{2}) - \frac{\beta}{\epsilon^3}(\phi_{i,j}^k - \frac{1}{2})^3 + \frac{\beta}{2\epsilon}\Delta\phi_{i,j}^k - \frac{12A\beta}{\epsilon}((\phi_{i,j}^k - \frac{1}{2})^3 - \nabla \cdot (|\nabla\phi_{i,j}^k|^2\nabla\phi_{i,j}^k)), \end{aligned} \tag{38}$$

$$\omega_{i,j}^{k+1} = \Delta\phi_{i,j}^{k+1}. \tag{39}$$

Note that this scheme is first order in time and second order in space. It follows that

Theorem 3.2. *Suppose that $\phi^{k+1}, \phi^k \in \mathcal{C}_{\tilde{m}\times\tilde{n}}$ and $\mathbf{n} \cdot \nabla_d \phi^{k+1} = 0$. The convex splitting scheme (37)–(39) is unconditionally energy stable, i.e., $F(\phi^{k+1}) \le F(\phi^k)$, independent of any choice of the time step size.*

Analogously, the fully discrete version of (29)–(31) is as follows:

$$\phi_{i,j}^{k+1} - \phi_{i,j}^k = \frac{S}{\epsilon}\nabla \cdot (M(\phi_{i,j}^k)\nabla \mu_{i,j}^{k+1}), \tag{40}$$

$$\begin{aligned} \mu_{i,j}^{k+1} = &\frac{\gamma(\mathbf{n}_{i,j}^k)}{\epsilon}(\phi_{i,j}^{k+1} - \frac{1}{2})^3 - \nabla \cdot (\epsilon\gamma(\mathbf{n}_{i,j}^k)\nabla\phi_{i,j}^{k+1}) + \frac{\beta}{2\epsilon^3}\Big(6(\phi_{i,j}^{k+1} - \frac{1}{2})^5 + \frac{1}{8}(\phi_{i,j}^{k+1} - \frac{1}{2})\Big) + \epsilon\beta\Delta\omega_{i,j}^{k+1} \\ &- \frac{6\beta}{\epsilon}(\phi_{i,j}^{k+1} - \frac{1}{2})\nabla(\phi_{i,j}^{k+1}\nabla\phi_{i,j}^{k+1}) + \frac{3\beta}{\epsilon}(\phi_{i,j}^{k+1} - \frac{1}{2})\Delta\phi_{i,j}^{k+1} \\ &+ \frac{12A\beta}{\epsilon}((\phi_{i,j}^{k+1} - \frac{1}{2})^3 - \nabla \cdot (|\nabla\phi_{i,j}^{k+1}|^2\nabla\phi_{i,j}^{k+1})) \\ &- \frac{\gamma(\mathbf{n}_{i,j}^k)}{\epsilon}(\phi_{i,j}^k - \frac{1}{2}) - \epsilon\nabla \cdot (\mathbf{P}\nabla_n\gamma(\mathbf{n}^k)|\nabla\phi^k|)_{i,j} - \frac{\beta}{\epsilon^3}(\phi_{i,j}^k - \frac{1}{2})^3 + \frac{\beta}{2\epsilon}\Delta\phi_{i,j}^k \\ &- \frac{12A\beta}{\epsilon}((\phi_{i,j}^k - \frac{1}{2})^3 - \nabla \cdot (|\nabla\phi_{i,j}^k|^2\nabla\phi_{i,j}^k)), \end{aligned} \tag{41}$$

$$\omega_{i,j}^{k+1} = \Delta\phi_{i,j}^{k+1}. \tag{42}$$

3.2.3. Space and time adaptive strategy

The fully coupled, discrete schemes (37)–(39) and (40)–(42) lead to a sequence of discrete elliptic equations at each time step. We shall solve them by using the adaptive multigrid method developed in [41,43,42,13]. In fact, since the system of governing equations is discretized on a block-structured Cartesian mesh, the composite mesh consists of a hierarchy of levels which is particularly suitable for adaptive multigrid. At each time step, we check grid cells for refinement using a simple undivided gradient test. Since it is essential that much more refinement is needed in the diffuse interface region. This test marks grid cells where the finite differences of the phase-field functions are large. In particular, the set of cell-centered points is marked for refinement in three dimensions if

$$\sqrt{(\phi_{i+1,j,k}-\phi_{i-1,j,k})^2+(\phi_{i,j+1,k}-\phi_{i,j-1,k})^2+(\phi_{i,j,k+1}-\phi_{i,j,k-1})^2} > C_k,$$

where C_k is the critical value for level k. More sophisticated mesh refinement strategy could also be used here [32] although by refining near the interface we automatically refine high curvature regions as well. See Fig. 9. For a detailed discussion of all the aspects of the adaptive algorithm, the reader is referred to [41].

Finally, although it is difficult to construct second-order convex splitting schemes for systems of such complexity as these, we can nevertheless generate second-order approximation using Richardson extrapolation to improve the accuracy. More precisely, we may compute two approximations ψ^s and $\psi^{s/2}$ at time t_l with time step sizes s and $0.5s$, respectively, and generate a second-order approximation as

$$\psi^{l,new} = 2\psi^{s/2} - \psi^s. \tag{43}$$

The results presented in Tables 2 and 3 confirm that the convex splitting scheme with Richardson extrapolation is second order accurate in time and in space.

In all our simulations presented in the next section, we use the fourth-order mobility $M(\phi) = 16\phi^2(1-\phi)^2$ [27,37]. To solve the nonlinear equations at the implicit time step a nonlinear multigrid method [42] is used.

4. Numerical results

In this section we present examples to show the robustness and effectiveness of the numerical schemes. First, we demonstrate the convergence and near optimal complexity of the solvers. Then we consider the dynamics in 2D and 3D of both the isotopic system ($\alpha = 0$) and the anisotropic system using several different initial interface shapes and anisotropies.

4.0.1. Complexity and convergence of the schemes

We use the initial condition given below in Eq. (44) to test the convergence rate and near optimal complexity of the numerical methods presented in the previous section. For the complexity test, we fix the time step size $s = 0.001$ and vary the spatial step sizes from $3.2/32$ to $3.2/512$, with each grid size being one half the size of the previous. Following [40], we vary the number of multigrid smoothing sweeps (λ). We report the results at $t = 0.02$. The number of multigrid iterations required to reduce the norm of the residual below the tolerance $T_{ol} = 1.0 \times 10^{-8}$ is given in Table 1, where we vary the parameters ϵ, λ and spatial step size h. We observe that for $\lambda = 2, 3$, the required number of iteration is nearly independent of h, which is also confirmed in Fig. 1, where the detailed residual values of the residuals for the different cases are described. The results suggest that the multigrid solver is of nearly optimal complexity.

$$\phi(x, y, t=0) = \frac{1}{2}\Big(1.0 - \tanh\Big(\frac{\sqrt{(x-1.6)^2+(y-1.6)^2}-0.8}{2\sqrt{2}\epsilon}\Big)\Big). \tag{44}$$

To estimate the convergence rate with respect to a mesh with grid spacing h, three different grid spacings $2h$, h, and $h/2$ are used. We calculate the error between two different grid spacings ϕ^h and $\phi^{h/2}$ by

$$e^{h:h/2}_{i,j} = \phi^h_{i,j} - \frac{1}{4}\Big(\phi^{h/2}_{2i,2j} + \phi^{h/2}_{2i-1,2j} + \phi^{h/2}_{2i,2j-1} + \phi^{h/2}_{2i-1,2j-1}\Big)$$

and correspondingly for $e^{2h:h}$. The rate of convergence is defined as

$$\log_2\Big(\frac{||e^{2h:h}||_2}{||e^{h:h/2}||_2}\Big).$$

For the convergence test, the mesh spacings are taken to be $h = \frac{3.2}{256}, \frac{3.2}{512}, \frac{3.2}{1024}$. We use the linear refinement path $s = 0.016h$. Therefore, the corresponding time step sizes $s = 0.0002, 0.0001, 0.00005$. The numerical results indicate that the scheme of convex splitting with Richardson extrapolation is indeed of second-order in both time and space, see Tables 2 and 3.

For the stability tests, we fix the mesh spacings $h = \frac{3.2}{256}$ and vary the time step sizes from 0.005 to 0.04, with each time step being double the size of the previous one. The parameters are $\epsilon = 0.03$, $\beta = 0.001$, $A = 1.0$. For the anisotropic case we

Table 1
The number of multigrid iterations required to reduce the norm of the residual below the tolerance $T_{ol} = 1.0 \times 10^{-8}$. The numbers are counted at time $t = 0.02$ with the time step size $s = 0.001$. The parameters are given in the text and in the table. The initial data are given below in Eq. (44). The detailed residual values for the different cases (labeled Tests) are given in Fig. 1. We find, for a variety of parameter sets, that the required number of multigrid iterations is nearly independent of the mesh size h by using the multigrid smoothing parameters $\lambda = 2, 3$.

		Test 1	Test 2	Test 3	Test 4	Test 5
	ϵ	0.2	0.2	0.2	0.1	0.05
	λ	1	2	3	3	3
h	3.2/32	7	5	5	4	5
	3.2/64	8	5	5	5	6
	3.2/128	8	6	5	5	6
	3.2/256	8	6	5	6	6
	3.2/512	9	6	5	6	7

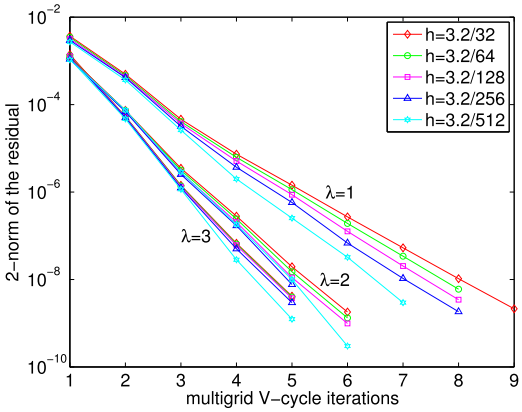

Fig. 1. 2-norm of the residual per multigrid V-cycle at time $t = 0.02$ with different smoothing parameter λ, i.e., $\lambda = 1, 2, 3$. The results showing the cases $\lambda = 2, 3$ achieve nearly optimal complexity of the solver (performance independent of grid size). See text for additional parameters and explanation.

Table 2
Errors and convergence rate for the scheme (37)–(39) of isotropic Cahn–Hilliard system with the Willmore regularization, combined with Richardson extrapolation. Parameters are $\epsilon = 0.03$, $\alpha = 0$, $\beta = 0.0001$, and the initial data are shown in Eq. (44). Numerical results confirm second order in time and space.

Grid sizes	256^2–512^2		512^2–1024^2
Error	4.268E-04		9.984E-05
Rate		2.09	

Table 3
Errors and convergence rate for the scheme (40)–(42) of strongly anisotropic Cahn–Hilliard system with the Willmore regularization, combined with Richardson extrapolation. Parameters are $\epsilon = 0.03$, $\alpha = 0.2$, $\beta = 0.0001$ and the initial data are shown in Eq. (44). Numerical results confirm second order in time and space.

Grid sizes	256^2–512^2		512^2–1024^2
Error	4.502E-03		9.269E-04
Rate		2.28	

choose the 4-fold anisotropy from Eq. (6) with $\alpha = 0.2$. Fig. 2 shows the discrete energy profiles for isotropic and strongly anisotropic systems. The discrete energy is non-increasing with any time step sizes. The results indicate that the schemes (37)–(39) and (40)–(42) for isotropic and anisotropic systems are both energy stable, even if this cannot be rigorously proved for the anisotropic case.

4.1. Coarsening dynamics

For the two dimensional examples shown here, the computational domain is $[0, 3.2] \times [0, 3.2]$. We choose the root-level grid size to be 32×32, and perform three levels of mesh refinement, i.e., the finest mesh size $h = 3.2/256$. We set time step

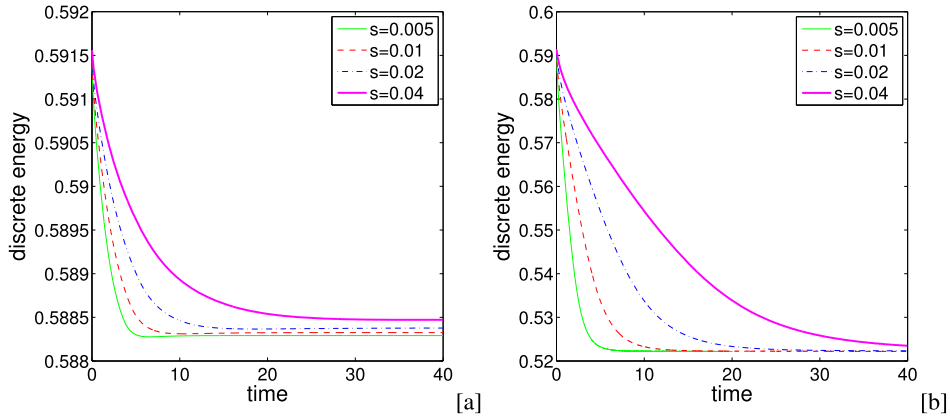

Fig. 2. Energy profile for isotropic system ($\alpha = 0$) [a] and strongly anisotropic system ($\alpha = 0.2$) [b] with different time step sizes. Other parameters are $\epsilon = 0.03$, $\beta = 0.001$, $A = 1.0$. In both cases, the energy monotonically decreases in time for any choice of time step.

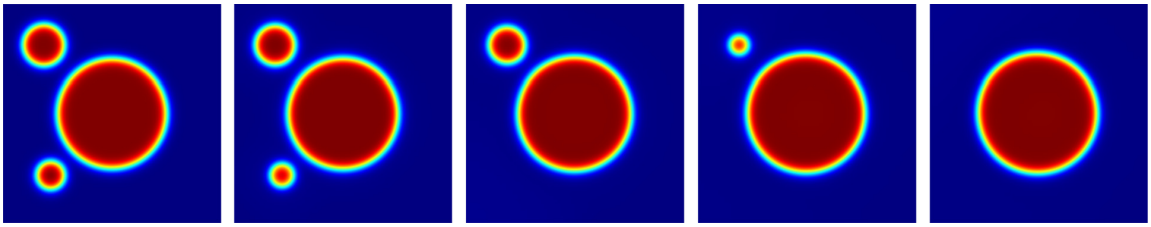

Fig. 3. Evolution of the phase function for the isotropic Cahn–Hilliard model with the Willmore regularization at $t = 0, 0.1, 0.3, 0.8, 1.0$, respectively. The parameters are given in the text.

size $s = 0.0001$, which is for the purpose of accuracy, not for the stability requirement, as the schemes are all unconditionally stable.

4.1.1. Isotropic case with the Willmore regularization

We here consider the isotropic Cahn–Hilliard system with the Willmore regularization. We use the following parameters:

$$\epsilon = 0.03,\ \beta = 0.004,\ \alpha = 0,\ A = 1.$$

Initial condition is

$$\phi(x, y, t = 0) = \prod_{i=1}^{3} \frac{1}{2}\Big(1.0 - \tanh\Big(\frac{\sqrt{(x - x_i)^2 + (y - y_i)^2} - r_i}{2\sqrt{2}\epsilon}\Big)\Big), \tag{45}$$

where $\{(x_i, y_i)\}_{i=1}^{3}$ and $\{r_i\}_{i=1}^{3}$ are circle centers and radii. We take $(x_1, y_1) = (0.6, 2.6)$, $(x_2, y_2) = (0.7, 0.7)$, $(x_3, y_3) = (1.6, 1.6)$, and $r_1 = 0.3, r_2 = 0.2, r_3 = 0.8$, respectively. The time evolution of the phase function ϕ is shown in Fig. 3 and the time evolution of the energy is shown in Fig. 4.

From Fig. 3, we can clearly see that the three circles undergo a coarsening process, in which two small circles are gradually absorbed into the large circle. Form Fig. 4, the total energy is seem to be monotonically decreasing with abrupt changes at the times $t = 0.3, 1.0$ at which the small circles disappear. At $t = 1.0$, the decrease in energy becomes fairly small and after some time the energy is almost constant.

4.1.2. Anisotropic case with the Willmore regularization

We now consider the anisotropic Cahn–Hilliard system with the Willmore regularization. We use the 4-fold anisotropy from Eq. (6) together with the following parameters:

$$\epsilon = 0.03,\ \beta = 0.004,\ \alpha = 0.2,\ A = 1.$$

The same initial condition is used as above for the isotropic system.

Fig. 5 shows the combined effects of anisotropy and coarsening. The three circles first evolve to anisotropic shapes with missing orientation at the four corners, then the anisotropic system coarsens and the small shapes disappear. Fig. 6 shows

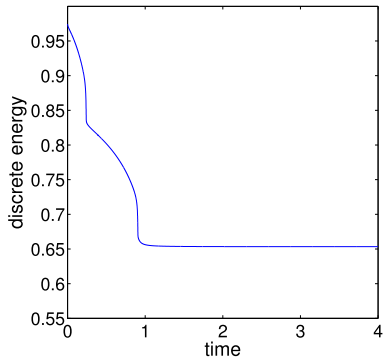

Fig. 4. Energy profile for the simulations shown in Fig. 3.

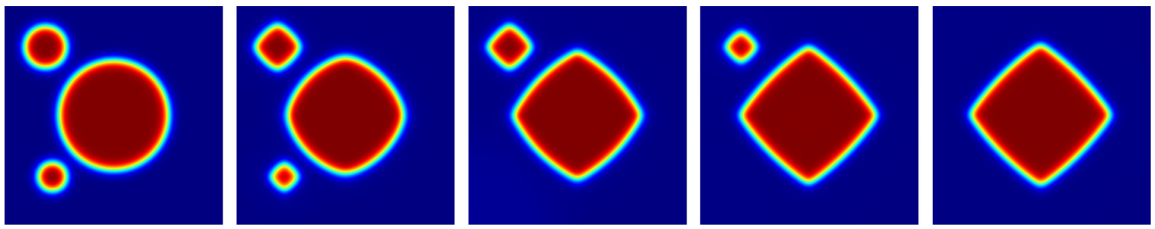

Fig. 5. Evolution of the phase function for the anisotropic Cahn–Hilliard model with the Willmore regularization at $t = 0, 0.1, 0.3, 1.0, 2.0$, respectively. The parameters are given in the text.

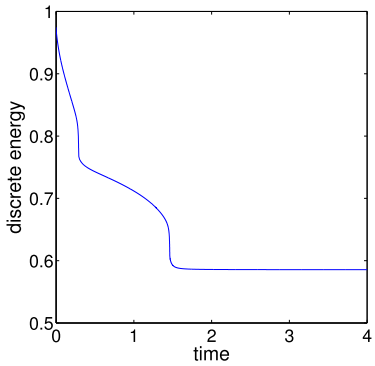

Fig. 6. Energy profile for the simulations shown in Fig. 5.

the energy profile. We observe that the total energy is decreasing and undergoes two rapid changes at $t = 0.3, 1.6$, which correspond to the times the small shapes disappear.

4.2. Anisotropy and missing orientations

In this section we study first the strong interfacial anisotropy of rough curve in two dimensions, then we investigate missing orientations in the Wulff shape and tetragonal trisoctahedron shape in three dimensions. We assess the effects of different α values and the Willmore regularization parameter β on the equilibrium interface morphologies.

4.2.1. Strong anisotropy of a rough curve

We now study the effects of the four-fold anisotropy on the dynamics of a rough curve. The computational domain is $[0, 6.4] \times [0, 3.2]$. The initial data is

$$\phi(x, y, t = 0) = \frac{1}{2}\Big(1.0 - \tanh\Big(\frac{y - 0.4 \times r(x) - 1.6}{2\sqrt{2}\epsilon}\Big)\Big), \tag{46}$$

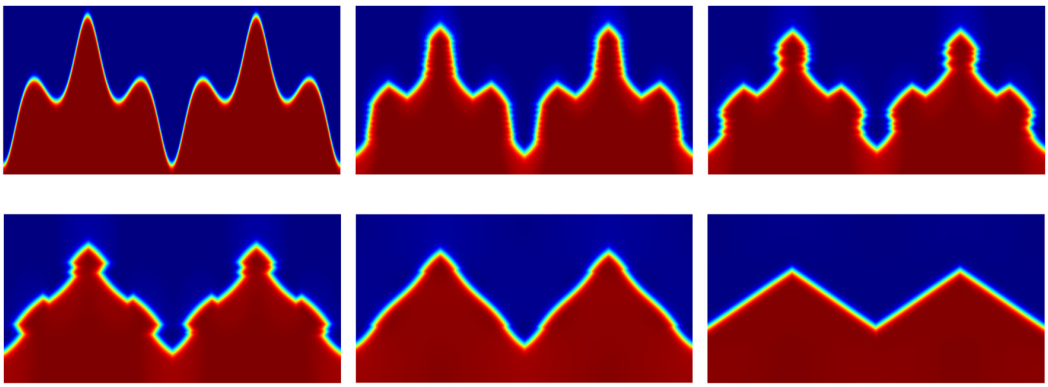

Fig. 7. Evolution of an initially rough surface undergoing decomposition into near-facets and kinks, followed by coarsening process due to strongly four-fold anisotropy. The parameters are given in the text.

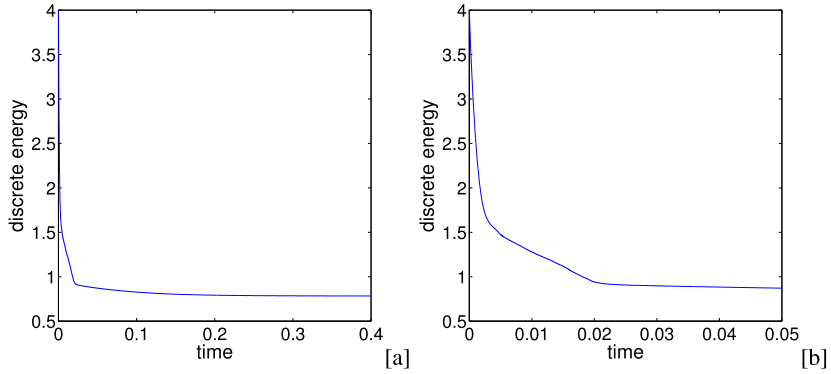

Fig. 8. [a]: Energy profile for the simulations shown in Fig. 7. [b]: A close-up showing where the energy decreases fast.

where

$$r(x) = 1.8\cos(\pi x) + 1.5\cos(3\pi x) + 0.2\cos(5\pi x) + 0.04\cos(7\pi x). \tag{47}$$

The domain is periodic in the x direction. The root-level grid has size 64×32, and three levels of mesh refinement are used. The time step size $s = 0.00001$ based on the accuracy requirement. The parameters are

$$\epsilon = 0.03,\ \beta = 0.0001,\ \alpha = 0.2,\ A = 1.0.$$

Fig. 7 shows the decomposition of an initially rough curve into near-facets and kinks followed by coarsening. The effect of the strongly four-fold anisotropy is clearly observed. Note that the shape is still evolving as the valley is being removed The dynamics of the energy are shown in Fig. 8; the energy is seen to be monotonically decreasing.

4.2.2. Missing orientations of the Wulff shape

We next investigate the effect of the strength of the four-fold anisotropy parameter α on crystal shapes in three dimensions. Four different values of α, i.e., $\alpha = 0.1, 0.2, 0.3, 0.4$, are considered. The other parameters $\epsilon = 0.03$, $\beta = 0.002$, and $A = 1$. Initial data is

$$\phi(x, y, z, t = 0) = \frac{1}{2}\left(1.0 - \tanh\left(\frac{\sqrt{(x-1.6)^2 + (y-1.6)^2 + (z-1.6)^2} - 0.8}{2\sqrt{2}\epsilon}\right)\right). \tag{48}$$

Which describes a sphere with radius $\sqrt{0.8}$. Two-levels of mesh refinement are used (see Fig. 9), where the root-level grid is $32 \times 32 \times 32$ and the time step size $s = 0.0001$. The evolution of the initially spherical shape towards its equilibrium is shown in Fig. 10, with $\alpha = 0.2$, and the corresponding two dimensional cross-sections along $x = 1.6$ are shown in Fig. 11. The results are in very good agreement with simulations shown in [35]. For different values of α, the equilibrium shapes are shown in Fig. 12, and the two dimensional cross-sections along $x = 1.6$ are shown in Fig. 13. It can be seen that as α is relatively small, such as $\alpha = 0.1$, missing orientations are not seen clearly. When α is increased ($\alpha = 0.2, 0.3, 0.4$),

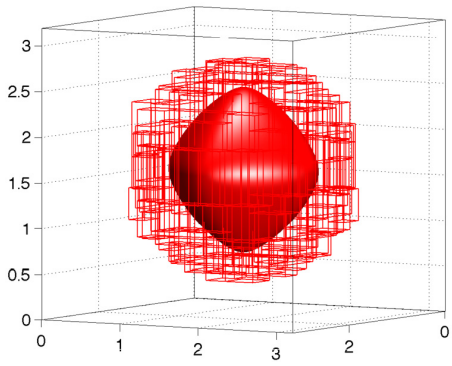

Fig. 9. A typical adaptive mesh from Fig. 12 with $\alpha = 0.2$ at $t = 0.1$. The $\phi = 0.5$ isosurface is shown. Two levels of refinement (red boxes) are performed with the root-level grid $32 \times 32 \times 32$ (not shown). (For interpretation of the colors in the figure(s), the reader is referred to the web version of this article.)

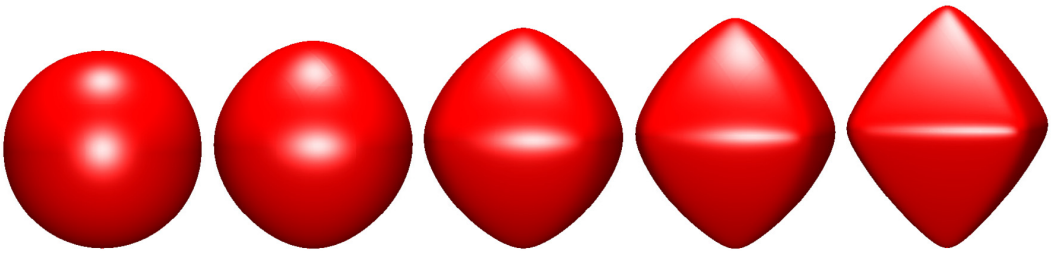

Fig. 10. Evolution of an initially spherical shape for the strongly anisotropic Cahn–Hilliard model with the Willmore regularization at $t = 0, 0.025, 0.1, 0.2, 2.0$, respectively. The parameters $\epsilon = 0.03$, $\alpha = 0.2$, $\beta = 0.002$, $A = 1.0$. The simulation is performed with two-levels of mesh refinement and the root-level grid is $32 \times 32 \times 32$.

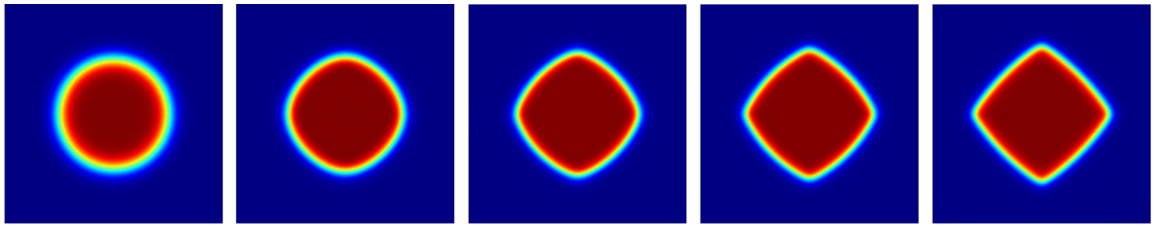

Fig. 11. Two-dimensional cross-section ($x = 1.6$) of the evolution from Fig. 10.

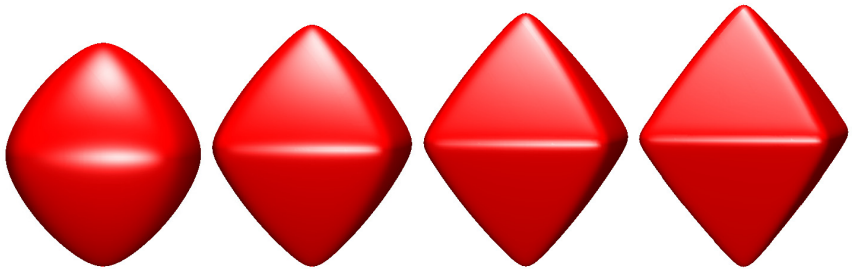

Fig. 12. Evolution of an initially spherical shape for the strongly anisotropic Cahn–Hilliard model with the Willmore regularization at $t = 2.0$, respectively. The parameters $\epsilon = 0.03$, $\beta = 0.002$, $A = 1.0$ with different α (from left to right): 0.1, 0.2, 0.3, and 0.4, respectively. See text for additional details.

shapes tend to be a double-sided pyramid because of the strong anisotropy. The energy profile (Fig. 14) shows that energy decreases faster with larger α.

The impact of the Willmore regularization parameter β on the equilibrium four-fold shapes is shown in Fig. 15; the two dimensional cross-sections along $x = 1.6$ are shown in Fig. 16. We take $\beta = 0.002, 0.004, 0.008, 0.01$. The other parameters

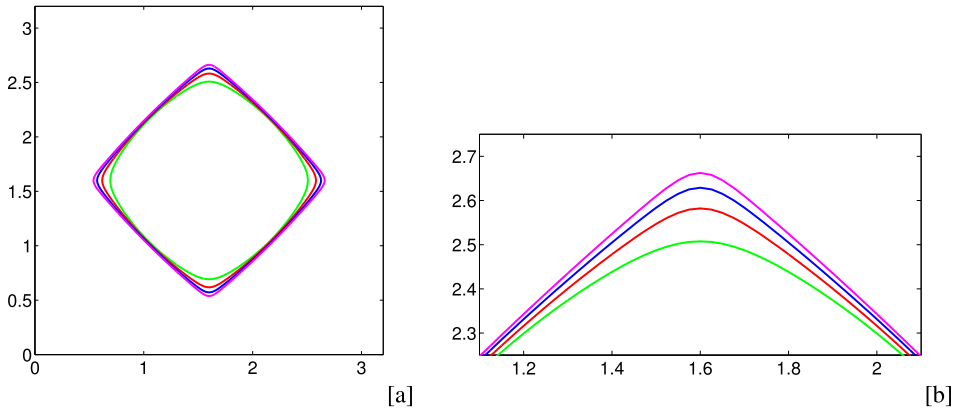

Fig. 13. Impact of the parameter α on the corner shape. [a]: Two-dimensional cross-section ($x = 1.6$) of the evolution of the initially spherical shape for the strongly anisotropic Cahn–Hilliard model with the Willmore regularization shown in Fig. 12. [b]: A close-up showing the upper corner with different α (from bottom to top): 0.1 (green), 0.2 (red), 0.3 (blue), and 0.4 (magenta). The parameters are given in the text.

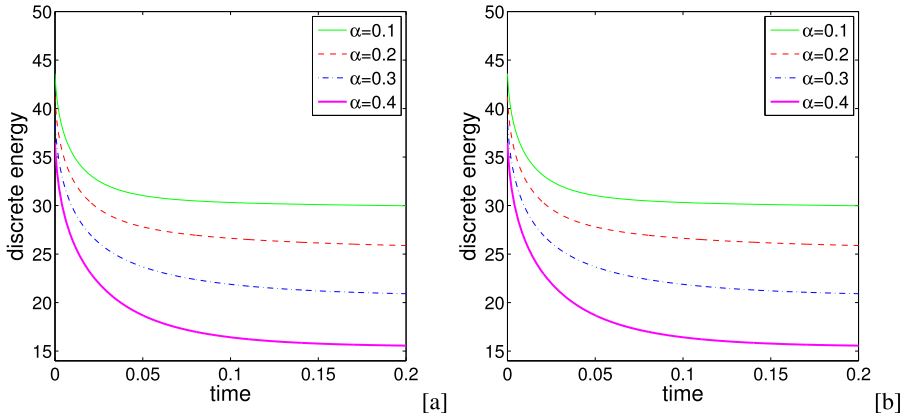

Fig. 14. Energy profile for the strongly anisotropic Cahn–Hilliard model with the Willmore regularization using four different values of α shown in Fig. 12. [b]: A close-up shows that energy decreases faster with larger α.

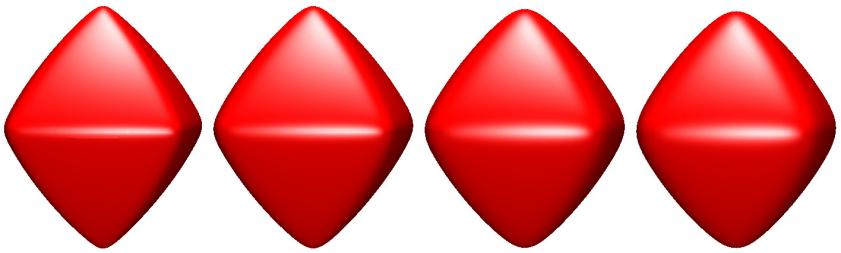

Fig. 15. Evolution of an initially spherical shape for the strongly anisotropic Cahn–Hilliard model with the Willmore regularization at $t = 2.0$, respectively. The parameters $\epsilon = 0.03$, $\alpha = 0.2$, $A = 1.0$ with different β (from left to right): 0.002, 0.004 , 0.008, and 0.01, respectively. See text for additional details.

$\epsilon = 0.03, \alpha = 0.2$, and $A = 1$. Two-levels of mesh refinement with a root-level grid of $32 \times 32 \times 32$ are used. The time step size $s = 0.0001$. It can be seen from Fig. 15 that the evolution from the initial sphere to the final Wulff shapes is similar to that shown in Fig. 10. As β increases, the corners are wider and smoother in the equilibrium morphologies. From the energy profile (Fig. 17) we can see that energy decreases faster with smaller β.

As a final example, we present the dynamics of an initial sphere (Eq. (48)) using an eight-fold symmetric anisotropic function [31,27]:

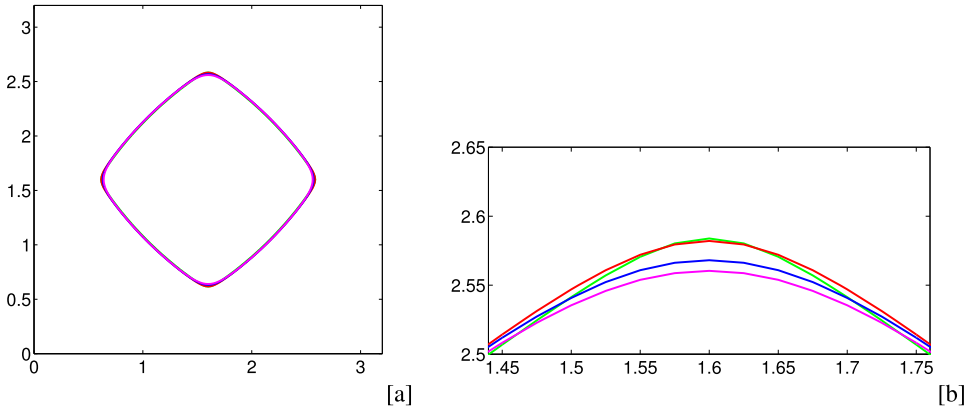

Fig. 16. Impact of the Willmore regularization parameter β on the corner shape. [a]: Two-dimensional cross-section ($x = 1.6$) of the evolution of the initially spherical shape for the strongly anisotropic Cahn–Hilliard model with the Willmore regularization shown in Fig. 15. [b]: A close-up showing the upper corner with different β (from top to bottom): 0.002 (green), 0.004 (red), 0.008 (blue), and 0.01 (magenta). Wider and smoother corners form in the equilibrium shapes as β increases. The parameters are given in the text.

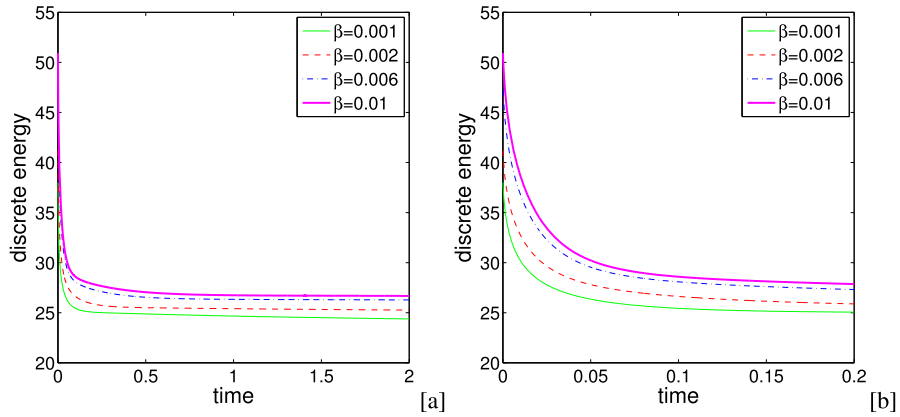

Fig. 17. [a]: Energy profile for the strongly anisotropic Cahn–Hilliard model with the Willmore regularization using four different values of β shown in Fig. 15. [b]: A close-up shows that energy decreases faster with smaller β.

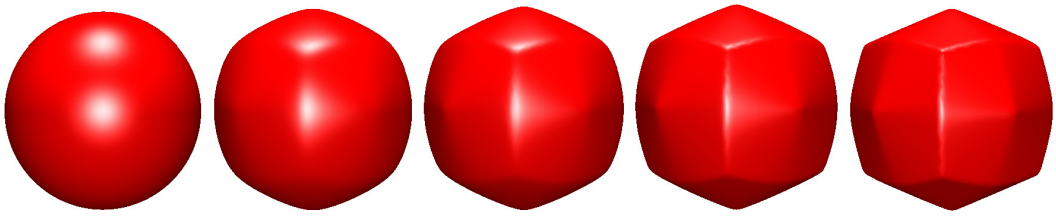

Fig. 18. Evolution of an initially spherical shape for the strongly anisotropic Cahn–Hilliard model with the Willmore regularization at $t = 0, 0.0025, 0.005, 0.01, 2.0$, respectively. The parameters $\epsilon = 0.03$, $\alpha = 0.2$, $\beta = 0.002$, $A = 1.0$. See text for additional details.

$$\gamma(\mathbf{n}) = 1 + \alpha\Big(4\sum_{i=1}^{d}(16n_i^8 - 20n_i^6 + 2n_i^4 + 3n_i^2) - 3\Big). \tag{49}$$

We take the parameters to be $\epsilon = 0.03$, $\alpha = 0.2$, $\beta = 0.002$, $A = 1.0$. Fig. 18 shows that facets are gradually formed from the crystal tends to its equilibrium shape – a tetragonal trisoctahedron. Two-levels of mesh refinement with a root-level grid of $32 \times 32 \times 32$ are used and the time step is $s = 0.0001$. Two-dimensional cross-sections along $x = 1.6$, presented in Fig. 19, show that the cross-sections acquire an octagonal shape.

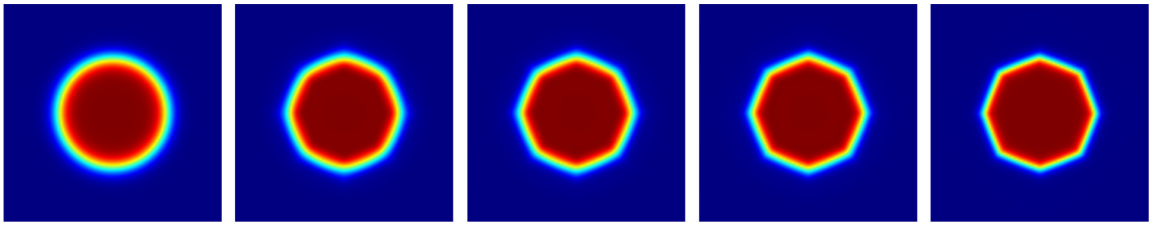

Fig. 19. Two-dimensional cross-section ($x = 1.6$) of the evolution of the initially spherical shape for the strongly anisotropic Cahn–Hilliard model with the Willmore regularization shown in Fig. 18.

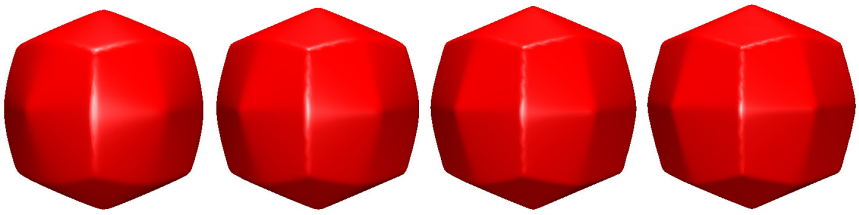

Fig. 20. Evolution of an initially spherical shape for the strongly anisotropic Cahn–Hilliard model with the Willmore regularization at $t = 2.0$, respectively. The parameters $\epsilon = 0.03$, $\beta = 0.002$, $A = 1.0$ with different α (from left to right): 0.1, 0.2, 0.3, and 0.4, respectively. See text for additional details.

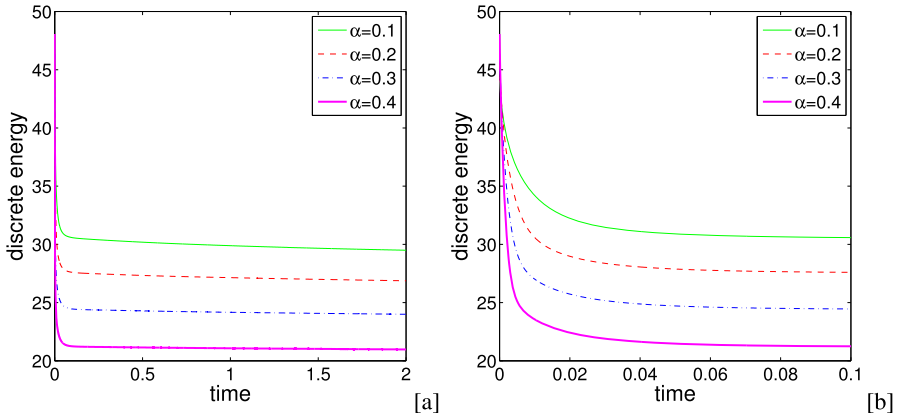

Fig. 21. [a]: Energy profile for the strongly anisotropic Cahn–Hilliard model with the Willmore regularization using four different values of α shown in Figs. 20. [b]: A close-up shows that energy decreases faster with larger α.

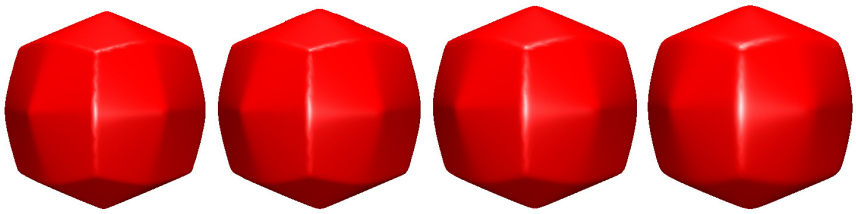

Fig. 22. Evolution of an initially spherical shape for the strongly anisotropic Cahn–Hilliard model with the Willmore regularization at $t = 2.0$, respectively. The parameters $\epsilon = 0.03$, $\alpha = 0.2$, $A = 1.0$ with different β (from left to right): 0.001, 0.002, 0.006 and 0.01, respectively. See text for additional details.

We next investigate the effect of α on the equilibrium morphologies. Fig. 20 shows for small anisotropies, such as $\alpha = 0.1$, the equilibrium shape tends to have rounded corners/edges. The stronger the anisotropy, the sharper the corner and edges become. The total energy of the system decreases as α increases, see Fig. 21. For fixed α, Fig. 22 shows that β enhances the degree of roundness of the corners/edges. The energy profile decreases as β decreases, see Fig. 23.

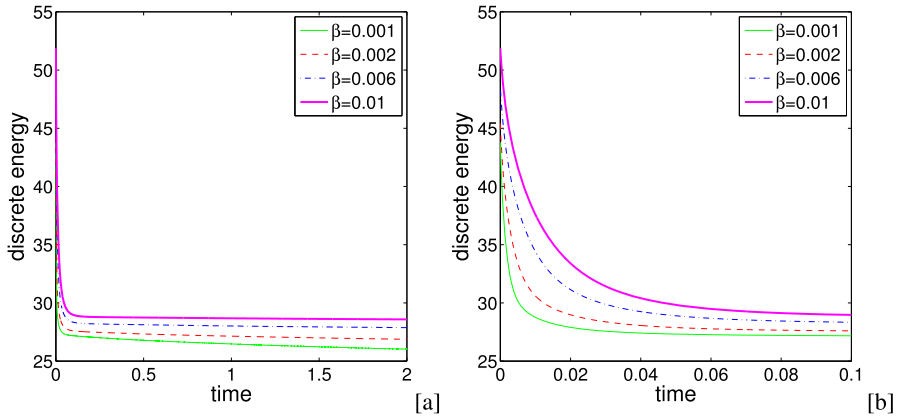

Fig. 23. [a]: Energy profile for the strongly anisotropic Cahn–Hilliard model with the Willmore regularization using four different values of β shown in Fig. 22. [b]: A close-up shows that energy decreases faster with smaller β.

4.3. Summary and future work

We have developed robust, efficient, and stable numerical methods to solve isotropic and strongly anisotropic Cahn–Hilliard systems with a Willmore regularization. These systems involve six order derivatives and are highly nonlinear. We used a convex splitting technique to develop energy stable schemes for the isotropic case and we extended this approach to account for anisotropy. Although we are not able to prove that the anisotropic scheme is energy stable, our numerical results indicates that even in the anisotropic case, the energy decreases for every choice of time step. To solve the nonlinear equations at the implicit time level, we used a very efficient adaptive nonlinear multigrid finite-difference algorithm. We validate our schemes by presenting some computational examples in both two and three dimensions, which exhibit excellent agreement with previous results by other methods. However, compared to previous approaches (e.g., [35]), we are able to use time steps that can be orders of magnitude larges.

We plan to extend the numerical approaches developed here to simulate other challenging mathematical models, such as a mathematical model of tumor growth which involves a Willmore energy to capture the dynamic evolution of basement membrane.

Acknowledgements

This work is partially supported by NSF DMS-1620262 (JS) and AFOSR FA9550-16-1-0102 (JS), NSF-DMS-1522775 (JL), NIH grant P50GM76516 (JL) for the Center of Excellence in Systems Biology at the University of California, Irvine, NSF-DMS 1418689 (CW), and NSF-DMS 1418692 (SW).

References

[1] S.M. Allen, J.W. Cahn, A microscopic theory for antiphase boundary motion and its application to antiphase domain coarsening, Acta Metall. Mater. 27 (1979) 1085–1095.
[2] V. Badalassi, H. Ceniceros, S. Banerjee, Computation of multiphase stems with phase field models, J. Comput. Phys. 290 (2003) 371–397.
[3] V. Badalassi, H. Ceniceros, S. Banerjee, Conservative multigrid methods for Cahn–Hilliard fluids, J. Comput. Phys. 193 (2004) 511–543.
[4] A. Baskaran, Z. Hu, J. Lowengrub, C. Wang, S. Wise, P. Zhou, Energy stable and efficient finite-difference nonlinear multigrid schemes for the modified phase field crystal equation, J. Comput. Phys. 250 (2013) 470–492.
[5] A. Baskaran, J. Lowengrub, C. Wang, S. Wise, Convergence analysis of a second order convex splitting scheme for the modified phase field crystal equation, SIAM J. Numer. Anal. 51 (2013) 2851–2873.
[6] M. Burger, F. Haußer, C. Stöcker, A. Voigt, A level set approach to anisotropic flows with curvature regularization, J. Comput. Phys. 225 (2007) 183–205.
[7] P.C. Bollada, P.K. Jimack, A.M. Mullis, Faceted and dendritic morphology change in alloy solidification, Comput. Mater. Sci. 144 (2018) 76–84.
[8] J.W. Cahn, J.E. Hilliard, Free energy of a nonuniform system I, interfacial free energy, J. Chem. Phys. 28 (1958) 258–267.
[9] J.W. Cahn, D.W. Hoffman, A vector thermodynamics for anisotropic surfaces–II, curved and faceted surfaces, Acta Metall. 22 (1974) 1205–1214.
[10] F. Chen, J. Shen, Efficient energy stable schemes with spectral discretization in space for anisotropic Cahn–Hilliard systems, Commun. Comput. Phys. 13 (2013) 1189–1208.
[11] Y. Chen, J. Lowengrub, Tumor growth in complex, evolving microenvironmental geometries: a diffuse domain approach, J. Theor. Biol. 361 (2014) 14–30.
[12] Y. Chen, J. Shen, Efficient, adaptive energy stable schemes for the incompressible Cahn–Hilliard Navier–Stokes phase-field models, J. Comput. Phys. 308 (2016) 40–56.
[13] Y. Chen, S. Wise, V. Shenoy, J. Lowengrub, A stable scheme for a nonlinear, multispecies tumor growth model with an elastic membrane, Int. J. Numer. Methods Biomed. Eng. 30 (2014) 726–754.
[14] A. DiCarlo, M. Gurtin, P. Podio-Guidugli, A regularized equation for anisotropic motion-by-curvature, SIAM J. Appl. Math. 52 (1992) 1111–1119.
[15] J.J. Eggleston, P.W. Voorhees, Ordered growth of nanocrystals via a morphologycal instability, Appl. Phys. Lett. 80 (2002) 306–308.

[16] J.J. Eggleston, G.B. McFadden, P.W. Voorhees, A phase-field model for highly anisotropic interfacial energy, Physica D 150 (2001) 91–103.
[17] D.J. Eyre, Unconditionally gradient stable time marching the Cahn–Hilliard equation, in: Computational and Mathematical Models of Microstructural Evolution, San Francisco, CA, 1998, Mater. Res. Soc. Symp. Proc., Warrendale, PA 529 (1998) 39–46.
[18] W. Feng, Z. Guan, J. Lowengrub, C. Wang, S.M. Wise, Y. Chen, A uniquely solvable, energy stable numerical scheme for the functionalized Cahn–Hilliard equation and its convergence analysis, J. Sci. Comput. (2018), https://doi.org/10.1007/s10915-018-0690-1.
[19] J.H. Garche, M. Rumpf, U. Weikard, The Cahn–Hilliard equation with elasticity: finite element approximation and qualitative studies, Interfaces Free Bound. 3 (2001) 101–118.
[20] S. Hu, L. Chen, A phase-field model for evolving microstructures with strong elastic inhomogeneity, Acta Mater. 49 (2001) 1879–1890.
[21] Z. Hu, S. Wise, C. Wang, J. Lowengrub, Stable and efficient finite-difference nonlinear-multigrid schemes for the phase-field crystal equation, J. Comput. Phys. 228 (2009) 5323–5339.
[22] J. Jou, P. Leo, J. Lowengrub, Microstructural evolution in inhomogeneous elastic media, J. Comput. Phys. 131 (1997) 109–148.
[23] J. Lowengrub, L. Truskinovsky, Quasi-incompressible Cahn–Hilliard fluids and topological transitions, Proc. R. Soc. Lond., Ser. A, Math. Phys. Eng. Sci. 454 (1998) 2617–2654.
[24] A. Makki, A. Miranville, Existence of solutions for anisotropic Cahn–Hilliard and Allen–Cahn systems in higher space dimensions, Discrete Contin. Dyn. Syst., Ser. S 9 (2016) 759–775.
[25] A. Miranville, Asymptotic behavior of a sixth-order Cahn–Hilliard system, Cent. Eur. J. Math. 12 (2014) 141–154.
[26] A. Rätz, A. Ribalta, A. Voigt, Surface evolution of elastically stressed films under deposition by a diffuse interface model, J. Comput. Phys. 214 (2006) 187–208.
[27] M. Salvalaglio, R. Backofen, R. Bergamaschini, F. Montalenti, A. Voigt, Faceting of equilibrium and metastable nano structures: a phase-field model of surface diffusion tacking realistic shapes, Cryst. Growth Des. 15 (6) (2015) 2787–2794.
[28] M. Salvalaglio, R. Backofen, A. Voigt, F. Montalenti, Morphological evolution of pit-patterned Si(001) substrates driven by surface-energy reduction, Nanoscale Res. Lett. 12 (2017) 554.
[29] R.F. Sekerka, Analytical criteria for missing orientations on three-dimensional equilibrium shapes, J. Cryst. Growth 275 (2005) 77–82.
[30] J. Shen, C. Wang, X. Wang, S. Wise, Second-order convex splitting schemes for gradient flows with Ehrlich–Schwoebel-type energy: application to thin film epitaxy, SIAM J. Numer. Anal. 50 (2012) 205–225.
[31] E.J. Siem, W.C. Carter, Orientation-dependent surface tension functions for surface energy minimizing calculations, J. Mater. Sci. 40 (2005) 3107–3113.
[32] M. Sussman, A.S. ALmgren, J.B. Bell, P. Colella, L.H. Howell, An adaptive level set approach for incompressible two-phase flows, J. Comput. Phys. 148 (1999) 81–124.
[33] J.E. Taylor, J.W. Cahn, Diffuse interface with sharp corners and facets: phase field models with strongly anisotropic surfaces, Physica D 112 (1998) 381–411.
[34] S. Torabi, J. Lowengrub, Simulating interfacial anisotropy in thin-film growth using an extended Cahn–Hilliard model, Phys. Rev. E 85 (2012) 041603.
[35] S. Torabi, J. Lowengrub, A. Voigt, S. Wise, A new phase-field model for strongly anisotropic systems, Proc. R. Soc. A 465 (2009) 1337–1359.
[36] T. Uehara, R.F. Sekerka, Phase field simulations of faceted growth for strong anisotropy of kinetic coefficient, J. Cryst. Growth 254 (2003) 251–261.
[37] A. Voigt, Comment on "Degenerate mobilities in phase field models are insufficient to capture surface diffusion" [Appl. Phys. Lett. 107 (2015) 081608], Appl. Phys. Lett. 108 (2016) 036101.
[38] C. Wang, X. Wang, S. Wise, Unconditionally stable schemes for equations of thin film epitaxy, Discrete Contin. Dyn. Syst., Ser. A 28 (2010) 405–423.
[39] C. Wang, S.M. Wise, An energy stable and convergent finite-difference scheme for the modified phase field crystal equation, SIAM J. Numer. Anal. 49 (2011) 945–969.
[40] S. Wise, Unconditionally stable finite difference, nonlinear multigrid simulation of the Cahn–Hilliard–Hele–Shaw system of equations, J. Sci. Comput. 44 (2010) 38–68.
[41] S. Wise, J.S. Kim, J. Lowengrub, Solving the regularized, strongly anisotropic Cahn–Hilliard equation by an adaptive nonlinear multigrid method, J. Comput. Phys. 226 (2007) 414–446.
[42] S. Wise, J. Lowengrub, V. Cristini, An adaptive multigrid algorithm for simulating solid tumor growth using mixture models, Math. Comput. Model. 53 (2011) 1–20.
[43] S. Wise, J. Lowengrub, J. Frieboes, V. Cristini, Three-dimensional multispecies nonlinear tumor growth – i: model and numerical method, J. Theor. Biol. 253 (2008) 524–543.
[44] S. Wise, J. Lowengrub, J. Kim, K. Thornton, P. Voorhees, W. Johnson, Quantum dot formation on a strain-patterned epitaxial thin film, Appl. Phys. Lett. 87 (2005) 133102.
[45] S. Wise, C. Wang, J. Lowengrub, An energy stable and convergent finite-difference scheme for the phase field crystal equation, SIAM J. Numer. Anal. 47 (2009) 2269–2288.
[46] P. Zhou, S. Wise, X. Li, J. Lowengrub, Coarsening of elastically stressed, strongly anisotropic driven thin films, Phys. Rev. E 85 (2012) 061605.